Materials Today Bio 21 (2023) 100722

Contents lists available at ScienceDirect

Materials Today Bio

journal homepage: www.journals.elsevier.com/materials-today-bio

Tumor-overexpressed enzyme responsive amphiphiles small molecular self-assembly nano-prodrug for the chemo-phototherapy against non-small-cell lung cancer

Peilian Liu [a,c,1], Yong Huang [c,1], Chenyue Zhan [d,*], Fu Zhang [d], Chuansen Deng [a], Yongmei Jia [a], Tao Wan [c], Sheng Wang [a,**], Bowen Li [b,c,***]

[a] School of Chemistry and Chemical Engineering, Key Laboratory of Clean Energy Materials Chemistry in Guangdong General University, Lingnan Normal University, Zhanjiang, 524048, PR China
[b] Department of Chemical and Biomolecular Engineering, National University of Singapore, 4 Engineering Drive 4, 117585, Singapore
[c] College of Pharmaceutical Sciences, Zhejiang University, Hangzhou, 310058, PR China
[d] Department of Hepatobiliary and Pancreatic Surgery, The First Affiliated Hospital, Key Laboratory of Combined Multi-Organ Transplantation, Ministry of Public Health, School of Medicine, Zhejiang University, Hangzhou, 310003, PR China

ARTICLE INFO

Keywords:
Nano-prodrug
NQO1-Responsive
Self-assembly
Amphiphiles small molecular
Combinational therapy

ABSTRACT

Rational design of self-assembly drug amphiphiles can provide a promising strategy for constructing nano-prodrug with high drug loading, smart stimuli-responsive drug release and high tumor selectivity. Herein, we report a small molecular amphiphile prodrug that can self-assemble into multifunctional nano-prodrug for enhanced anticancer effect by the combination of chemotherapy and phototherapy (PDT/PTT). In this prodrug, the simple insertion of quinone propionate into hydrophilic drug Irinotecan (Ir) generates suitable amphiphiles that endow a good self-assembly behavior of the prodrug and transform it into a stable and uniform nanoparticle. Interestingly, this excellent self-assembly behavior can load phototherapy agent ICG to form a multifunctional nano-prodrug, thereby enhancing the chemotherapeutic effect with PDT/PTT. Importantly, the quinone propionic acid moiety in the prodrug showed a high sensitivity to the overexpressed NAD(P)H:quinone oxidoreductase-1 (NQO1) in non-small cell lung cancer (NSCLC) cells, and this sensitivity enables the disassembly of nano-prodrug and efficient NQO1-responsive drug release. To further enhance the drug accumulation on tumor tissue and migrate the blood clearance, a biomimetic nano-prodrug has been successfully explored by coating hybrid membrane on the above nano-prodrug, which displays high selective inhibition of tumor growth and metastasis on NSCLC mice model. Our findings provide new insights into the rational design of tumor-overexpressed enzyme responsive nano-prodrug for cancer combinational therapy.

1. Introduction

Prodrugs have offered significant opportunities for stimuli-responsive drug release in tumor microenvironment (TME) that can effectively facilitate the therapeutics effect of anticancer drugs by relieving the severe side-effect, multi-drug resistance (MDR) and poor pharmacokinetics [1–5]. Early work in anti-cancer prodrug research mainly focused on the chemical modification with TME-responsive group (lower pH, overexpressed enzymes and oxygen/reductive species, *etc.*) on small molecular chemotherapeutics, and boosted the development of a number of small molecular prodrugs that exhibited high specificity and good therapeutic effect on cellular and even sub-cellular levels [6–9]. However, the *in vivo* drug delivery of these small molecular prodrugs is rather difficult due to short-time systemic circulation and poor *in vivo* targeting ability [10,11]. For small molecular prodrug, expanding from cellular and sub-cellular level to living animals is a fascinating and important frontier, as prodrug in living animals has great potential for controlled drug release and for relieving MDR and side-effect [12,13]. Thus, nano-prodrug may be

* Corresponding author. Department of Chemical and Biomolecular Engineering, National University of Singapore, 4 Engineering Drive 4, 117585, Singapore.
** Corresponding author. Department of Chemical and Biomolecular Engineering, National University of Singapore, 4 Engineering Drive 4, 117585, Singapore.
*** Corresponding author. Department of Chemical and Biomolecular Engineering, National University of Singapore, 4 Engineering Drive 4, 117585, Singapore.
E-mail addresses: 0620778@zju.edu.cn (C. Zhan), dyesws@126.com (S. Wang), bowen_86@nus.edu.sg (B. Li).
[1] These authors contributed to the work equally and should be regarded as co-first authors.

https://doi.org/10.1016/j.mtbio.2023.100722
Received 8 May 2023; Received in revised form 20 June 2023; Accepted 1 July 2023
Available online 4 July 2023

considered as a promising strategy to overcome the shortcoming on *in vivo* drug delivery of small molecular prodrug [14,15]. Using nano-carrier to deliver the small molecular prodrug is an attractive measure for enhancing the drug accumulation into tumor site and maintaining stability on the systemic circulation [16–19]. To date, a variety of nano-carriers, such as polymer, inorganic materials, and biomimetic materials *etc.*, have been exploited to load prodrug or modify with small molecular drug by TME-responsive linkage so as to achieve efficient drug delivery in live animals [20–24]. However, these nano-carriers often display some non-ignorable disadvantages, including the toxicity and side-effect of the carrier, poor loading efficiency, and premature drug leakage [25–27]. Thus, designing a nano-prodrug delivery system that exhibits more high-efficiency and safe remains challenging on this issue so far.

The small molecular self-assembly strategy has been explored to integrate the advantages of free-carrier and prodrug, which is capable of low excipient-related toxicity with high drug loading and good tumor selectivity [28]. Recently, many works focused on the strategies to covalently use the sulfur or selenium bond as a linkage, which formed a homodimeric prodrug that could self-assemble into a stable nanoparticle under physiological conditions [29–33]. In these nano-prodrugs, the disulfide, diselenide or trisulfide bond not only serves as a GSH/ROS-responsive bond to trigger the prodrug, but also plays an important role in self-assembly behavior due to the enhancements of the flexibility in prodrug. On the other hand, the rational design of small molecular drug amphiphiles can endow good self-assembly behavior to form nanostructures and expand the scope of nano-prodrug beyond GSH/ROS-responsive trigger, as well as bring about new approaches for other activation and drug release [34–36]. Interestingly, this self-assembly nano-prodrug can also load the conjugated drug molecule by hydrophobic, hydrogen-bond and π-π interactions [37]. This additional function is able to incorporate drugs or imaging agents and other therapeutics into an "all-in-one" nano-prodrug and achieve the combination therapy to improve the therapeutic effects.

Among TME-responsive activation, overexpressed enzymes were found to exhibit high selectivity and incomparable specificity for triggering prodrug [38,39]. Yan and co-workers first reported an esterase-responsive amphiphilic nano-prodrug for cancer combination therapy, yet limited success has been achieved in its further application due to the high level of esterase in other organ tissues resulting in relative low specificity [36]. However, to the best of our knowledge, TME overexpressed enzymes with high specificity as a trigger in nano-prodrug are rarely reported. NQO1 (also called DT-diaphorase, EC 1.6.99.2) is a cytoplasmic dielectron oxidoreductase that catalyzes the reduction of various quinone compounds to corresponding phenols [40]. Solid evidence proved that NQO1 is overexpressed in a variety of tumors, such as non-small-cell lung cancer (NSCLC), which is up to 80 times more than that of normal tissue [41]. Recently, many NQO1 substrates have been explored as a trigger group for activating the prodrug in the treatment of tumors with overexpression of NQO1 [42,43]. Quinone propionate is a high specificity and easily available NQO1 substrate that used as an ideal trigger for designing the NQO1 nano-prodrug [44]. In addition, the long chain structure and hydrophobicity of quinone propionate may provide an opportunity for the successful construction of a self-assembly nano--prodrug, achieving the NQO1-responsive drug release.

Phototherapy, including photothermal therapy (PTT) and photodynamic therapy (PDT), has aroused great interest because of its non-invasion, maneuverability, and minimal dark toxicity in cancer treatment [45]. Some small molecule phototherapy agents had been approved to apply in clinic treatment, such as indocyanine green (ICG), Chlorine e6 (Ce6), magnesium deoxychlorate (PA) and porphyrin as phototherapy agents, but their inferior systemic circulation and lacking of targeting ability severely limit its output of the therapeutic effects. Based on these findings, small molecule phototherapy agents have been modified by means of nano-formulation, which has paved the way for enhanced their therapeutic effect and biosafety. Among various nanoforms, the nanodrug based on cell-membrane-based biomimetic strategies have received extensive attention due to their good ability to reduce the clearance of reticuloendothelial system and enhance tumor targeting [46,47]. Especially in hybrid membrane-coated nanodrug, the hybrid membrane that prepared by the mixed remodeling of different cell membranes can simultaneously achieve the above multiple functions, such as homologous targeting toward tumors through the homing effect of cancer cell membranes and immune escape through macrophage cell membranes [48].

Herein, we have developed an NQO1-responsive amphiphiles self-assembly nano-prodrug, CM-ICG@IrQ, that can achieve the co-delivery of the chemotherapeutics and phototherapy (PDT/PTT) agent in combination therapy of NSCLC, as shown in Scheme 1. In small molecular formulations, this prodrug consists of a chemotherapeutics Ir and an NQO1-responsive quinone propionic acid, and this simple insertion of a hydrophobic quinone propionate can transform the hydrophilic Ir into a stable and uniform nanoparticle by the formation of amphiphile. Interestingly, the phototherapy agent ICG can be loaded into this nanoparticle during the self-assembly process and form a multifunctional nano-prodrug (ICG@IrQ). In TME, the disassembly behavior of ICG@IrQ can be triggered by the overexpression of NQO1, resulting in the Ir activation and the NQO1-responsive release of ICG. This NQO1-responsive drug release can generate the combined therapeutic effect of chemotherapeutics and PDT/PTT on tumor tissue as opposed to normal tissue, effectively mitigating the serve side-effect of Ir and ICG. Furthermore, ICG@IrQ was coated with the related cancer cell-macrophage hybrid membrane (A549/RAW 264.7) on its surface and formed a biomimetic nano-prodrug (CM-ICG@IrQ) with two highlights: low reticuloendothelial system clearance and high tumor targeting. In addition, the drug release behavior, biodistribution, tumor inhibition and anti-metastasis were also clarified on the NSCLC mouse model. This study might provide a simple and high-efficiency nano-prodrug for combination therapy on NSCLC.

2. Experimental section

2.1. Fabrication of nano-prodrugs IrQ NPs and ICG@IrQ

IrQ (5 mg) was dissolved in 200 μL of DMSO, then slowly added to deionized water (5 mL) and vigorously stirred for 30 min, followed by dialyzing (MWCO 1000 Da) in deionized water for one day, with the deionized water being exchanged every 6 h to obtain self-assembled nano-prodrug IrQ NPs. IrQ (5 mg) and ICG (5 mg) were dissolved in 200 μL of DMSO, stirred evenly, and then added gradually to 5 mL of deionized water for 30 min to make the nano-prodrug ICG@IrQ. Then the nano-prodrug ICG@IrQ was obtained by using the dialysis method described above.

2.2. Preparation of hybrid cell-membrane coated nano-prodrugs CM-ICG@IrQ

The cell membrane extraction and fusion were prepared using protocol-reported with a little modification. Briefly, the A549 cells and RAW 264.7 cells were separately collected and treated with EDTA-free protease inhibitor in PBS buffer. Then, the cell suspensions were treated with ultrasonic for 5 min and centrifuged for 10 min (700 g, 4 °C). After that, a new centrifuge tube was used to carefully collect the supernatant, which was then centrifuged for 30 min (14000 g, 4 °C) to obtain cell membranes. For membrane fusion, the obtained two precipitates were re-suspended at the same weight ratio in 200 μL of buffer solution, then sonicated for 3 min. Subsequently, the polycarbonate porous membrane (400 nm) was employed to extrude the sample and facilitate membrane fusion. Finally, the collected hybrid membrane vesicles were stored for later use. To prepare the hybrid cell-membrane

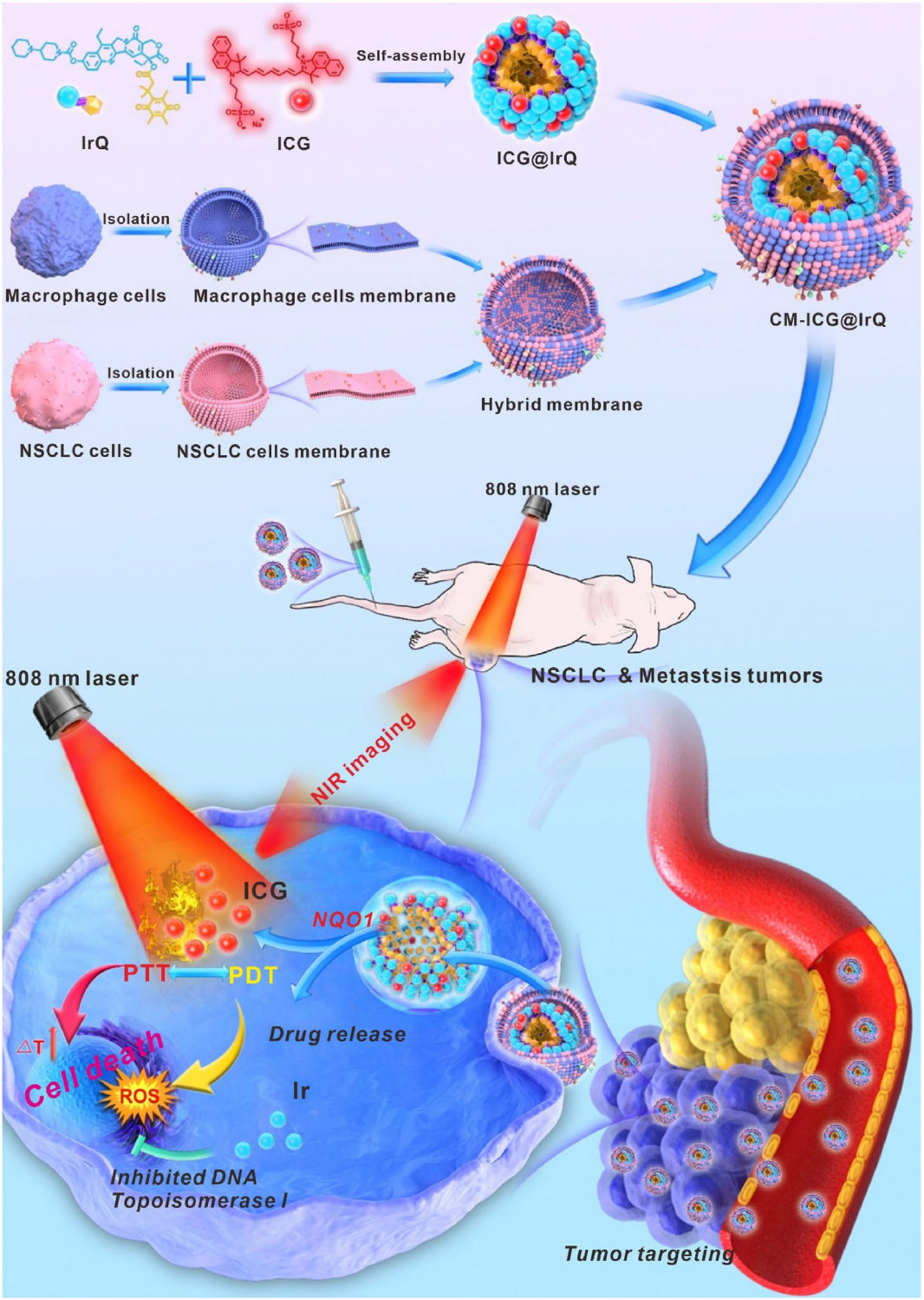

Scheme 1. Schematic illustration of the fabrication of nano-prodrugs CM-ICG@IrQ and the chemo-phototherapy against NSCLC by NQO1-responsive drug release.

coated CM-ICG@IrQ nano-prodrugs, 1 mg of hybrid membrane in buffer was added into ICG@IrQ solution, then sonicated (0 °C for 2 min). Later on, this mixture was extruded to obtain the biomimetic nano-prodrugs CM-ICG@IrQ through a 250 nm polycarbonate membrane. The CM-ICG@IrQ was then characterized by DLS, TEM, and SDS-PAGE. The DLE (drug loading efficiency) was determined by the formula: DLE = WD/WN × 100%, WD: the weight of encapsulated drug, WN: the weight of nanoparticles).

2.3. Critical aggregation concentration (CAC) measurement

Pyrene was used as a probe based on its fluorescence characteristic for determining the CAC value of the IrQ. By adding 3 μL of pyrene solution (6×10^{-4} mol L^{-1}) in acetone to 3 mL of IrQ aqueous at different concentrations, the concentration of pyrene was maintained at 6×10^{-7} mol L^{-1}. With an excitation light at 335 nm, the fluorescence emission spectra of each sample were examined. The third emission peak (I_3) and the first emission peak (I_1) of each sample were recorded.

2.4. In vitro drug release assay

The dialysis method was employed to study the release properties of ICG and Ir *in vitro*. The ICG@IrQ solution (5 mL, 1 mg mL^{-1}) was encapsulated in dialysis bags (MWCO 3500 Da) and dialyzed in PBS (50 mL) containing a certain amount of NQO1 (0–50 μg mL^{-1}). Later on, for HPLC testing, 200 μL of buffer solution was exchanged with the same amount of fresh buffer at 0, 1, 2, 4, 8, 12, and 24 h, and the release amount was calculated using the standard curve of ICG and Ir, and the drug release curve was drawn. For HPLC testing, peaks of IrQ and Ir in the chromatograms were detected by monitoring the absorption at 370 nm, and peaks of ICG by monitoring the absorption at 790 nm. The mobile phase was acetonitrile/water (40/60) at a flow rate of 1.0 mL/min. All the tests were performed in triplicate.

2.5. In vitro photothermal studies

Firstly, we recorded the temperatures of PBS, IrQ NPs, ICG, ICG@IrQ, and CM-ICG@IrQ solution for 5 min with laser irradiation. Next, we discussed the effect of concentration on temperature. Different CM-ICG@IrQ concentrations (ICG-equivalent concentration: 0, 10, 25, 50 μg mL^{-1}) were prepared and then irradiated for 5 min. To test the photothermal stability of CM-ICG@IrQ, CM-ICG@IrQ solution (ICG-equivalent concentration: 25 μg mL^{-1}), which was continuously exposed to the laser for 5 min, then stop irradiation for 5 min, repeated five times. Temperature changes were measured by a photothermal camera.

2.6. Determination of reactive oxygen production

1,3-Diphenylisobenzofuran (DPBF, reactive oxygen species probe) was chosen to study the production of ROS, and IrQ NPs (44 μg mL^{-1}), ICG (25 μg mL^{-1}), ICG@IrQ (ICG-equivalent concentration: 25 μg mL^{-1}) and CM-ICG@IrQ (ICG-equivalent concentration: 25 μg mL^{-1}) were suspended in PBS buffer containing 10 μM DPBF, respectively. The mixture was then placed in a cuvette and irradiated for 8 min. For measuring the absorption spectroscopy (UV–vis) of DPBF to evaluate the level of ROS production by the reduction of its absorption intensity at 410 nm.

2.7. Cell viability assay

Fresh medium containing ICG, IrQ NPs, ICG@IrQ, and CM-ICG@IrQ (IrQ-equivalent concentration: 0–50 μg mL^{-1}) was used for cell culture for 48 h. In the inhibition of NQO1, A549 cells were pretreated with dicoumarol (5 μM) for 1 h, then treated with relevant nano-prodrugs. For phototoxicity, cells were irradiated for 5 min after 4 h incubation, and then further incubated for 44 h. Afterward, the cells were cultured with CCK8 reagent for 3 h and measured via a microplate reader. Especially, the PBS group was selected as the negative group of cytotoxicity and the cell viability was set as 100%. All groups were tested in eight replicates.

2.8. Cellular imaging for cellular uptake, ROS analysis and live/dead cell staining assay

For cellular uptake analysis, A549 cells (2×10^5 per dish) were seeded on 35 mm confocal dishes and incubated overnight. Then, the cells were treated with free ICG, ICG@IrQ, and CM-ICG@IrQ (ICG-equivalent concentration: 7.75 μg mL^{-1}) for 1, 2, and 4 h. Then cells were rinsed for CLSM imaging.

In order to measure the ROS generation in A549 cells, the ROS Assay Kit was used. Briefly, A549 cells were firstly washed with PBS buffer after incubating various formulations for 4 h. The medium containing the DCFH-DA (10 μM) from the ROS assay kit was then added, followed by 30 min incubation. After irradiation for 5 min, the cells were washed and imaged by CLSM.

For live/dead cell staining assay, the cell seeding, incubation mode, and drug concentration were the same as the cell apoptosis assay. After incubation, the live and dead cell assay was treated with Calcein/PI cell viability/cytotoxicity assay kit on the basis of the suggested protocol and imaged by a fluorescence microscope.

2.9. Cell apoptosis analysis

Cells were treated with ICG, IrQ NPs, ICG@IrQ, and CM-ICG@IrQ (ICG-equivalent concentration: 5.7 μg mL^{-1}; IrQ-equivalent concentration: 10 μg mL^{-1}) for 48 h, respectively. The cells in the laser irradiation groups were subjected to irradiate for 5 min. The cell apoptosis was evaluated according to the Annexin V-FITC/PI Kit protocol.

2.10. Animal model

The Animal Center of Zhejiang Academy of Medical Sciences provided the 6–8 weeks female BALB/c-nude mice. All animal experiments were performed in compliance with the requirements of the Animal Experimental Ethical Committee of Zhejiang University (Permit No: 2020–1561). We first established an A549 xenograft nude mice model by subcutaneously injecting A549 cells (2×10^6) into the right hind limb. After 7 days, the mice were split up into 6 groups ($n = 5$) at random: (G1) PBS, (G2) ICG + L, (G3) IrQ NPs, (G4) ICG@IrQ, (G5) ICG@IrQ + L, and (G6) CM-ICG@IrQ + L for *in vivo* antitumor efficiency of CM-ICG@IrQ. To establish A549 lung metastasis model, the BALB/c nude mice were injected with the suspension of A549-Luci cells (1×10^6 cells) via the tail vein. After one day, 6 groups of mice with the same as the above model were randomly assigned.

2.11. In vivo fluorescence imaging

A549 subcutaneous xenograft model on mice were constructed first. When the volume of tumors reached ≈150 mm^3, the mice were treated with ICG, ICG@IrQ, and CM-ICG@IrQ (ICG dose: 1 mg kg^{-1}) via the way of tail vein injection. Mice were anesthetized and taken images at various points of time (0, 1, 2, 4, 8, 12, 24, and 48 h) after the injection. After *in vivo* imaging, the mice were sacrificed immediately, and tumor tissues and major organs (heart, lung, liver, kidney, and spleen) were obtained for *ex vivo* imaging.

2.12. In vivo photothermal imaging

Mice with tumors were subjected to tail intravenous injection of PBS, the ICG@IrQ, and CM-ICG@IrQ (ICG dose: 2 mg kg^{-1}), separately. Twelve hours later, the tumor sites were irradiated for 5 min, and the temperature of tumor was recorded with a photothermal camera.

2.13. In vivo pharmacokinetics studies

Tumor-bearing mice were administrated with CM-ICG@IrQ (1 mg kg^{-1}) intravenously. At predetermined time points (0, 1, 2, 4, 8, 12, 24, and 48 h), the mice were sacrificed, and the blood samples were collected, heparinized, and centrifuged to afford the plasma. The major organs were dissected out and weighed. The obtained organs and plasma were suspended in acetonitrile and then homogenized and filtered. The concentrations of Ir and IrQ were determined by HPLC according to corresponding standard curves.

2.14. In vivo antitumor activity

For antitumor therapy studies, we first established an A549 xenograft nude mice model by subcutaneously injecting A549 cells (2×10^6) into the right hind limb. 7 days later, the mice were split up into 6 groups ($n = 5$) at random: (G1) PBS, (G2) ICG + L, (G3) IrQ NPs, (G4) ICG@IrQ, (G5) ICG@IrQ + L, and (G6) CM-ICG@IrQ + L. Formulations were intravenously administrated every three days for a total of five times with equal

amounts of ICG (2 mg kg^{-1}) and IrQ (3.5 mg kg^{-1}). After 12 h of the injection, laser irradiation on the tumor region of mice was performed. The body weights were measured every two days for 24 days. According to the formula: V = (length) × $(width)^2/2$, the tumor volume (V) was calculated. Then, the mice in each group were sacrificed, and the tumors were excised and weighed. Besides, hematoxylin and eosin (H&E) staining of the tumor tissues and major organs was implemented.

The A549 lung metastasis model was established to study the anti-metastasis effect of the nano-prodrugs. The BALB/c nude mice were injected with the suspension of A549-Luci cells (1×10^6 cells) via the tail vein. After one day, 6 groups of mice with the same as the above model were randomly assigned. The different formulations (the dose of ICG and IrQ were 2 mg kg^{-1} and 3.5 mg kg^{-1}) were injected intravenously every three days for a total of five times from day 0 to day 12, and laser irradiation on the tumor region of mice was administrated after 12 h of the injection. The Caliper IVIS spectroscopy, a non-invasive bioluminescence imaging system based on luciferase, was used to monitor the growth of lung metastases after injection with 2 mg of D-fluorescein potassium salt (200 μL, 10 mg mL^{-1}) 10 min before imaging on days 4, 12, and 21, respectively. After 21 days of treatment, the HE staining assay was performed on the major organ of the euthanized mice, and the lung tumor nodules were fixed, photographed, and counted. In addition, body weights were recorded during the period of treatment, and the survival rates of the different treatment groups were studied for up to 45 days.

3. Results and discussion

3.1. Preparation, characterization and in vitro drug release behavior of IrQ NPs

The synthesis route of the small molecular prodrug IrQ was first depicted in Fig. S1. We used EDC as condensation agent to obtain small molecular prodrug IrQ by covalent bonding between irinotecan (Ir, a DNA Topoisomerase I inhibitor) and quinone propionate through esterification reaction, and the structure of IrQ was confirmed by nuclear magnetic resonance (^1H and ^{13}C) and high-resolution mass spectrometry (HR-MS) (Figs. S2–S4). In this prodrug, quinone propionate could be used not only as pharmacological passivating group, but also as NQO1-responsive trigger for drug release. Due to the perfect drug amphiphiles (hydrophilicity of Ir and hydrophobicity of quinone propionate), IrQ might generate an outstanding self-assembly behavior and self-assembled into a stable nanoparticle in aqueous solution. As shown in Fig. 1A I. and 1 B, we first investigated the self-assembly behavior of IrQ, and found that it was able to form a stable nanoparticle (IrQ NPs) under physiological conditions by a simple and convenient nanoprecipitation method. Regular spherical morphology from IrQ NPs was obtained by transmission electron microscopy (TEM), and dynamic light scattering (DLS) revealed that the hydration diameter of IrQ NPs was about 162.7 nm with good dispersion (PDI = 0.105), and an obvious Tyndall effect could be observed in Fig. 1B. In addition, we further evaluated the stability of IrQ NPs after long-time storage (15 days), which was no significant changes in particle size and PDI value within 15 days (Fig. S5). To investigate this self-assembly performance resulting from the rational amphiphile of the small molecule IrQ, the critical aggregation concentration (CAC) was measured with pyrene-based fluorescence method. As shown in Fig. 1C, the critical aggregation concentration (CAC) of IrQ was as low as 1.276 μg mL^{-1}, which fully verified the excellent self-assembly ability of IrQ.

Many works proved that quinone propionate group can quench the emission of a fluorophore by PET effect [6,38,49]. As expected, the fluorescence was quenched when Ir was covalently linked to quinone propionate, and recovered in the presence of NQO1 (Fig. S6), and therefore, the fluorescence recovery of Ir could act as a continuous quantitative signal to monitor the NQO1-responsive Ir release. After verifying the fluorescence responsiveness of IrQ NPs, we investigated the concentration-dependent response of IrQ NPs to NQO1 by fluorescence spectroscopy. As shown in Fig. 1D and Fig. S7, with the increase of NQO1 concentration, the fluorescence intensity continued to enhance and reached a plateau at 25 μg mL^{-1}. We also found that the fluorescence changes of IrQ NPs showed a time dependence on NQO1 (Fig. S8). Subsequently, the qualitative analysis of NQO1-responsive release was performed by HPLC. As shown in Fig. 1E, the peak of IrQ (retention time 32.13 min) gradually decreased with the increase of NQO1 (0–50 μg mL^{-1}), and a new peak (retention time 15.37 min) appeared and enhanced concurrently, which was in good agreement with the peak of Ir (retention time 15.37 min). The release behavior was also proved by high-resolution mass spectrometry (HR-MS) titration (Fig. S9). The related results were corresponding with our hypothetical NQO1-responsive mechanism as depicted in Fig. S10. To further investigate the NQO1-responsive performance of IrQ NPs under physiological conditions, the selectivity and anti-interference behavior of IrQ NPs was examined in complicated biological environments. As shown in Figs. S11 and S12, we found that IrQ NPs exhibited splendid stability in the presence of common amino acids and metal ions, and could be activated by NQO1 in a wide pH range (4–8). In addition, the particle size and morphology change of IrQ NPs under NQO1 provided the additional evidences for the NQO1-responsive performance (Fig. S13). All these results clearly indicated that IrQ NPs exhibited excellent NQO1 responsiveness.

3.2. Preparation, characterization and in vitro drug release behavior of ICG@IrQ

The combination of chemo-phototherapy has shown great potential in anticancer treatment, especially in alleviating the chemo-resistance of chemotherapeutics. Indocyanine green (ICG) is an FDA-approved near-infrared contrast agent, which can not only be used as a fluorescence imaging agent to monitor drug distribution *in vivo*, but also be widely used as a phototherapy (PDT/PTT) agent. More importantly, the suitable conjugate structure of ICG may provide the possibility to load it into IrQ NPs and form multifunctional nano-prodrugs. Thus, we attempted to load ICG into IrQ NPs for constructing an "all-in-one" nano-prodrug ICG@IrQ that could achieve the combination of chemo-phototherapy. As depicted in Fig. 1A II., ICG@IrQ was prepared by a nanoprecipitation method due to the prominent and stable self-assembly of IrQ. To select suitable feeding ratio of ICG and IrQ, we investigated the average particle size, drug loading, encapsulation rate and product stability at the different feeding ratio, which found that the feeding ratio of 1:1 feature relatively high loading and good stability (Table S1 and Fig. S14). We first characterized ICG@IrQ by UV–vis absorption spectroscopy. The UV–vis spectrum of ICG@IrQ displayed the characteristic peaks of IrQ and ICG, proving that ICG was successfully loaded (Fig. 1F). Subsequently, TEM analysis showed that ICG@IrQ displayed regular spherical morphology (Fig. 1G). Compared with IrQ NPs, the hydration diameter of ICG@IrQ was slightly larger (179.2 nm) with better dispersion (PDI = 0.064), and also displayed obvious Tyndall effects and stable drug storage (Fig. S15). We further explored the possible mechanism of IrQ NPs loading ICG. Since Triton X-100, urea, and sodium chloride are thought to weaken hydrophobic interaction, hydrogen bonding, and electrostatic interactions, respectively, we added these species to ICG@IrQ to test their capacities to disorganize the nanoparticles. As shown in Fig. S16, Triton X-100 showed a significant ability to disintegrate nanoparticles because of hydrophobic competition, while urea and sodium chloride had negligible effects on nanoparticles, suggesting that the mechanism of IrQ NPs loading ICG could be attributed to hydrophobic interactions. Encouraged by this successful construction of ICG@IrQ, HPLC was carried out to study its release behavior in the presence of NQO1. In Fig. 1H, the release rate of Ir showed a concentration-dependent of NQO1 and the release rate of Ir increased rapidly with the increasing NQO1. The release rate of Ir reached a plateau within 4 h with a release rate close to 80% at 50 μg mL^{-1} of NQO1. Meanwhile, we found that the release rate of ICG also showed a dependence on the concentration of NQO1 (Fig. 1I), which

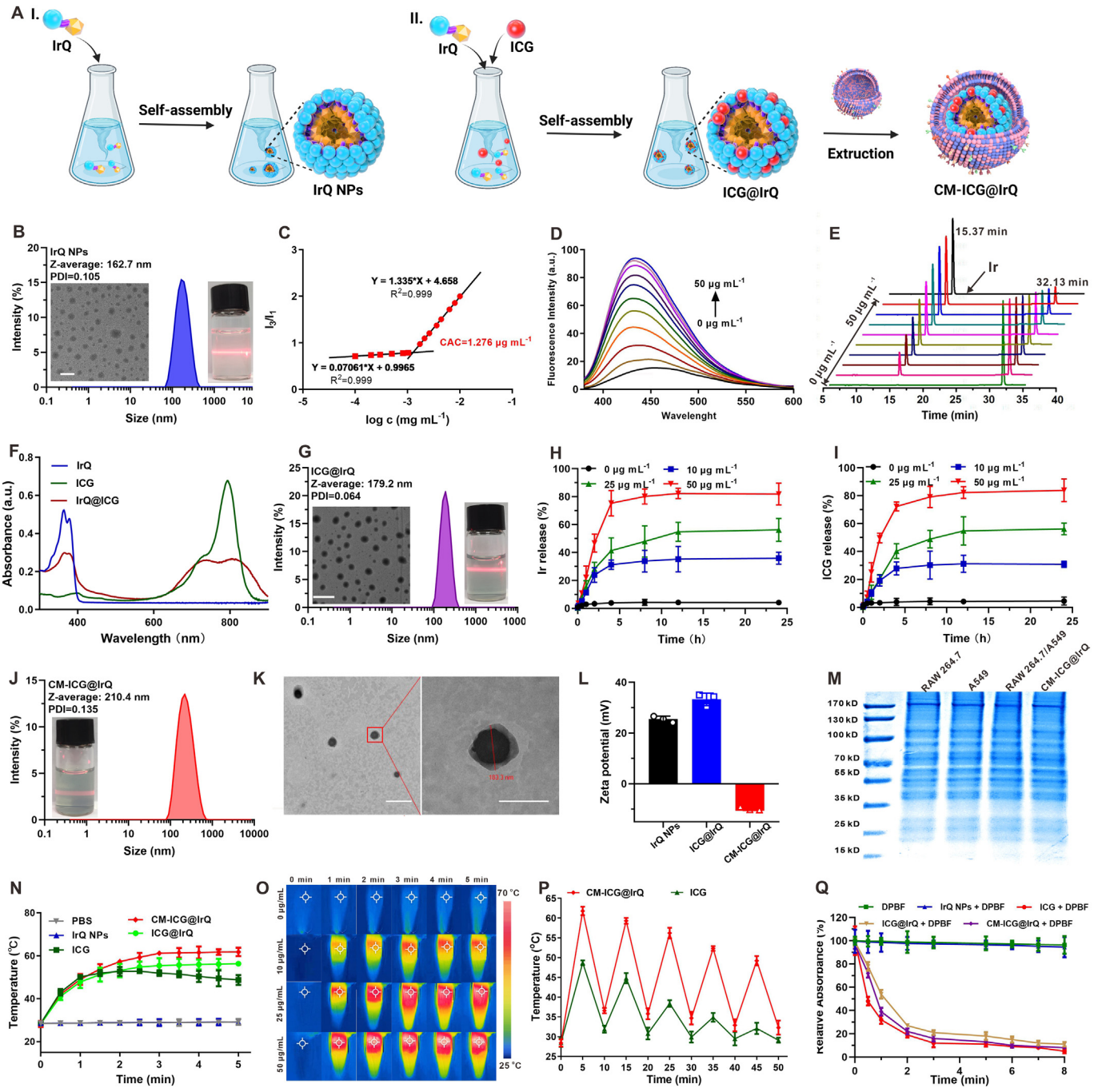

Fig. 1. (A I.) Schematic preparation of IrQ NPs. (A II.) Schematic preparation of CM-ICG and CM-ICG@IrQ (II). (B) TEM, DLS and Tyndall effect of IrQ NPs; TEM image scale bar: 200 nm. (C) Correlation between intensity ratio of the third and first fluorescence emission peak (I_3/I_1) of pyrene and the concentration of IrQ in water. (D) Fluorescence variation of IrQ upon incubation with NQO1 (0–50 μg mL^{-1}). (E) HPLC curves of IrQ treated with NQO1 (0–50 μg mL^{-1}), and HPLC curve of Ir (black line). (F) Absorption spectra of IrQ NPs, ICG and ICG@IrQ. (G) TEM, DLS and Tyndall effect of ICG@IrQ; TEM image scale bar: 500 nm. (H and I) Cumulative Ir and ICG release profiles from ICG@IrQ treated with NQO1 (0, 10, 25 and 50 μg mL^{-1}) n = 3. (J) DLS and Tyndall effect of CM-ICG@IrQ. (K) TEM images of CM-ICG@IrQ; scale bar: 500 nm for left, 200 nm for right. (L) Zeta potential of IrQ NPs, ICG@IrQ and CM-ICG@IrQ, n = 3. (M) SDS-PAGE membrane protein analysis from RAW264.7 macrophage cells, A549 cells, RAW264.7 & A549 hybrid membranes and CM-ICG@IrQ (hybrid membrane-coated). (N) Temperature-time curves of PBS, IrQ NPs, ICG, ICG@IrQ and CM-ICG@IrQ under irradiation with an equivalent ICG concentration of 25 μg mL^{-1}, n = 3. (O) Infrared thermal images of CM-ICG@IrQ with different equivalent ICG concentrations (0, 10, 25 and 50 μg mL^{-1}) under irradiation for 5 min. (P) Temperature curves of CM-ICG@IrQ and free ICG (ICG-equivalent concentration: 25 μg mL^{-1}) for five irradiation/cooling cycles, n = 3. (Q) Analysis of ROS production capacity of various formulations. Laser irradiation conditions in all experiments: 808 nm, 1 W cm^{-2}, n = 3. Data represent mean ± SD.

had a similar release curve to Ir. We investigated the release property of Ir and ICG form ICG@IrQ at different pH. As shown in Fig. S17, we found that Ir and ICG could be released in the presence of NQO1 in a wide pH range (4–8). In addition, the release behavior of ICG@IrQ was also determined by DLS and TEM, and we found that the structure of ICG@IrQ was dissociated under the action of NQO1 with large size (average 717 nm) and irregular morphology (Fig. S18).

3.3. Preparation, characterization and in vitro drug release behavior of CM-ICG@IrQ

To alleviate clearance by the reticuloendothelial system and enhance the tumor targeting capability during systemic circulation, we further coated the cancer cell-macrophage hybrid membrane (A549 and RAW 264.7 cells) on ICG@IrQ to construct biomimetic nano-prodrug CM-ICG@IrQ (Fig. 1A II). To confirm the successful fusion of A549 and RAW 264.7 cell membranes, we stained A549 and RAW 264.7 cell membranes with Lectin-FITC and Dil, respectively, and then mixed them to prepare hybrid membranes for imaging by confocal fluorescence microscopy. As shown in Fig. S19, we found that the fluorescence of the two channels overlaps good, indicating their successful fusion for subsequent coating application. As shown in Fig. 1J, the DLS test of CM-ICG@IrQ suggested a low PDI value with significant Tyndall effect after hybrid membrane coating, and the hydration diameter increased from 179.2 nm to 210.4 nm, which was consistent with the TEM observation (Fig. 1K). Moreover, the drug loading efficiency of IrQ and ICG were determined to be 50.8 and 29.1 wt%, respectively. The IrQ NPs and ICG@IrQ showed a positive Zeta potential (Fig. 1L). After coating to form CM-ICG@IrQ, the Zeta potential dropped from 33 mV to −10.8 mV, which further confirmed the presence of a negatively charged cell membrane layer. The coating of the cell membrane was also demonstrated by protein analysis. As shown in Fig. 1M, the protein bands of CM-ICG@IrQ were nearly similar to those of native membrane and hybrid membrane. We next evaluated the NQO1-responsive behavior of the biomimetic nano-prodrug CM-ICG@IrQ, as shown in Figs. S20 and S21, the release rates of Ir and ICG in CM-ICG@IrQ were positively correlated with the concentration of NQO1 concentration. In the absence of NQO1, CM-ICG@IrQ remained stable with negligible release of Ir and ICG. The release of Ir and ICG reached a plateau within 8 h in the presence of 50 μg mL^{-1} of NQO1 with a release rate at about 80%. The DLS showed that the hydration diameter rapidly increased to about 500 nm after incubation with NQO1 (Fig. S22). Expectedly, no regular spherical morphology was observed by TEM, indicating the collapse of the CM-ICG@IrQ nanostructure. The above data indicated that we have successfully constructed a hybrid membrane coated bionic nano-prodrug CM-ICG@IrQ with excellent response to NQO1.

3.4. The photothermal properties and ROS production of CM-ICG@IrQ

To evaluate the photothermal properties of CM-ICG@IrQ, we used an infrared thermal imaging system to monitor the real-time temperature upon uninterrupted laser irradiation (808 nm, 1 W cm^{-2}). As shown in Fig. 1N, the temperature of CM-ICG@IrQ increased promptly from 28.3 °C to 61.4 °C and then tended to equilibrium within 3 min. After 5 min of irradiation, ICG@IrQ and CM-ICG@IrQ reached 56.3 and 61.8 °C, respectively. At the initial stage, the heating rate of the free ICG was slightly faster than that of the nano-prodrugs containing ICG. However, after 1 min of irradiation, the heating rate of the free ICG slowed down obviously, and the temperature reached the maximum value in about 2 min, then displayed a downward trend, and finally reached only 48.7 °C. The main reasons for the higher peak temperatures of ICG@IrQ and CM-ICG@IrQ than free ICG may be the robust self-assembly properties of IrQ and the coating of hybrid membranes that improve the stability of ICG and increase ICG monomers within nanoparticles [50,51]. We further investigated the relationship between the concentration of CM-ICG@IrQ and its photothermal behavior. As shown in Fig. 1O and Fig. S23, CM-ICG@IrQ showed a clear concentration-dependence temperature increase upon irradiation (808 nm, 1 W cm^{-2}). The temperature of CM-ICG@IrQ at 25 μg mL^{-1} (ICG-equivalent concentration) exceeded 60 °C after 5 min of irradiation, and that at 50 μg mL^{-1} (ICG-equivalent concentration) exceeded 70 °C. By contrast, the control group (PBS) exhibited negligible temperature change during irradiation. The photothermal conversion efficiency of CM-ICG@IrQ was calculated to be 22.81%, which was higher than that of many reported ICG-based nanoparticle photothermal agents (Table S2). In addition, to compare the photostability of the free ICG and CM-ICG@IrQ, we irradiated them for 5 min, then natural cooling for 5 min, and repeated this cycle 5 times. As shown in Fig. 1P, CM-ICG@IrQ still had good photothermal capacity and stability after five cycles, and the temperature still reached 49.3 °C after the 5th irradiation. However, the temperature rise of free ICG after two cycles was very limited, and the temperature could only rise to 32.1 °C during the 5th irradiation. As we know, ICG displays satisfactory PDT effect by remarkable ROS production in anti-cancer treatment. To evaluate the ROS generation behavior of our biomimetic nano-prodrug, 1, 3-diphenylisobenzofuran (DPBF, the reduction of UV absorption at around 410 nm) was served as ROS probe to determine the ROS production under irradiation. The DPBF alone and IrQ NPs showed no significant decrease in UV absorption (Fig. 1Q). In striking contrast, the UV absorption of ICG@IrQ and CM-ICG@IrQ groups was significantly decreased. The DPBF in these two groups was almost completely degraded, which was comparable to the level of the free ICG group, indicating that ICG@IrQ and CM-ICG@IrQ could rapidly generate abundant ROS under irradiation. All the above results reliably demonstrated that CM-ICG@IrQ features conspicuous photothermal and photodynamic properties.

3.5. The cell uptake and intracellular release behavior of CM-ICG@IrQ

The good cell uptake of nano-drugs is the prerequisite for effective treatment, and the cellular uptake behavior of our biomimetic nano-prodrug (CM-ICG@IrQ) was assessed by the fluorescence properties of ICG. First, the localization of the CM-ICG@IrQ was clarified. As shown in Fig. S24, the results of organelle co-localization showed that the CM-ICG@IrQ were located in the cytoplasm. The A549 cells were treated with ICG, ICG@IrQ and CM-ICG@IrQ for 1, 2, and 4 h and then imaged. Strong fluorescence was observed after the incubation of ICG@IrQ and CM-ICG@IrQ for 2 h, which increased with the extension of incubation time (Fig. 2A). However, only weak fluorescence was observed at various observation time points in the free ICG, indicating that ICG@IrQ and CM-ICG@IrQ were more readily taken up by cells than ICG. Moreover, at each observation time point, the fluorescence of the CM-ICG@IrQ group was stronger than that of the ICG@IrQ group, demonstrating that the coating of the hybrid membrane could improve the cell uptake of nano-prodrug and facilitate its internalization by the enhancement of homologous targeting.

A549 cells, as one of NSCLC cells, have the natural characteristic of NQO1 overexpression, which served as an ideal model to explore the intracellular Ir releasing from CM-ICG@IrQ. As shown in Fig. 2B, the blue fluorescence from Ir rapidly enhanced with increasing incubation time, which was in good agreement with the extracellular NQO1-responsive fluorescence restoration, indicating that CM-ICG@IrQ was activated to release the active drug Ir. As control, A549 cells were pretreated with dihydroxycoumarin (an NQO1 inhibitor) to inactivate NQO1, as shown in Fig. S25, only negligible fluorescence was observed even at 4 h of incubation, which proved that NQO1 was highly specific for the drug release of CM-ICG@IrQ. Moreover, the release behavior of CM-ICG@IrQ in normal cell LO2 (NQO1 low-overexpressed) was also investigated to verify its selectivity. We found that relatively weak red fluorescence from ICG and negligible blue fluorescence from Ir were observed after 4 h of incubation with CM-ICG@IrQ (Fig. S26), which was attributed to the insignificant level of NQO1 in normal cells and poor drug release of CM-ICG@IrQ. These results suggested that CM-ICG@IrQ displays good specificity and high-efficient release in NQO1-overexpressed cancer cells.

To evaluate the PDT effect of CM-ICG@IrQ, we explored the intracellular ROS production with DCFH-DA (a ROS sensor). As shown in Fig. 2C, relatively weak green fluorescence could be detected after the treatment of free ICG with laser irradiation (ICG + L). Moreover, the IrQ NPs or ICG@IrQ without irradiation also displayed poor ROS production, and by contrast, A549 cells treated with CM-ICG@IrQ with irradiation (CM-ICG@IrQ + L) showed the strongest green fluorescence, indicating

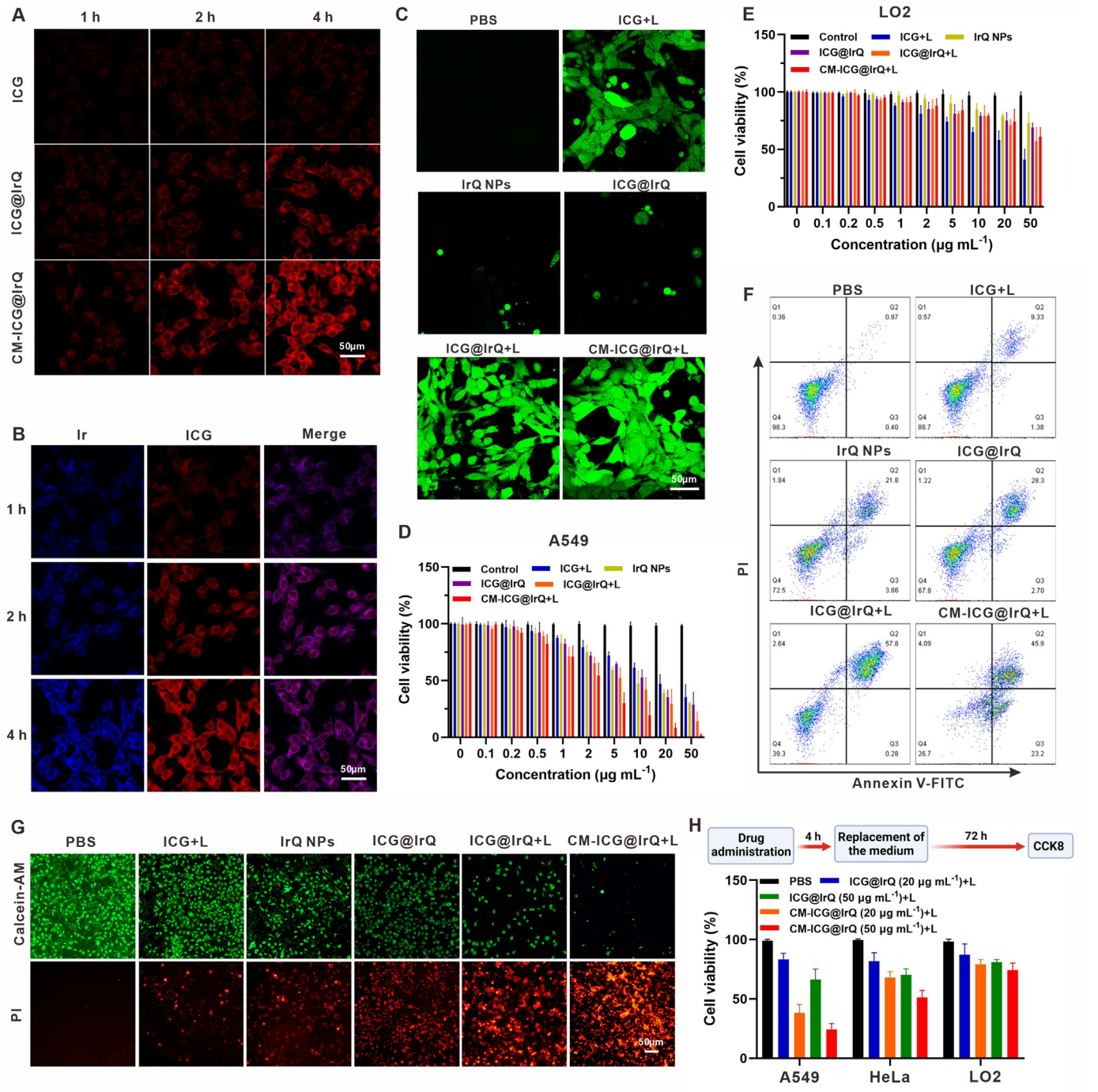

Fig. 2. (A) A549 cells treated with free ICG, ICG@IrQ and CM-ICG@IrQ for 1, 2, and 4 h before confocal laser scanning microscopy imaging (CLSM) (excitation: 633 nm). (B) A549 cells treated with CM-ICG@IrQ for 1, 2, and 4 h before CLSM (excitation: 405 nm for Ir channel, 633 nm for ICG channel). (C) ROS generation of various formulations with or without irradiation. (D–E) CCK8 assays of A549 cells and LO2 cells under the treatment of various formulations with or without irradiation. (F) Annexin VFITC/Propidium Iodide (PI) apoptosis assay of various formulations on A549 cells. (G) Live/dead imaging of A549 cells under the treatment of different formulations. (H) Cell viability of A549, HeLa and LO2 cells treated with ICG@IrQ and CM-ICG@IrQ based on short-term drug administration, n = 8.

the largest amount of ROS generation. These observations directly demonstrated that the homologous targeting properties conferred by the hybrid membrane significantly improved the PDT effects of the nano-prodrug system.

Having confirmed the ability of the nano-prodrugs to release drugs and induce ROS production in NQO1-overexpressed cancer cells, we next set out to explore their cytotoxicity by CCK8 assays. As depicted in Fig. 2D, the ICG + L and IrQ NPs showed moderate toxicity at all test concentrations. The CM-ICG@IrQ + L was the most toxic to A549 cells due to its combination of PDT/PTT and chemotherapy, as well as homologous targeting. It showed significant toxicity at low concentrations as low as 2 μg mL^{-1}, with a survival rate around 55%, and the cell viability rapidly decreased to 11% at 50 μg mL^{-1}. Along with A549 cells, HeLa cells with high expression levels of NQO1 were also used to reveal the toxicity of our nano-prodrugs, and the toxicity of them on HeLa cells was similar to that on A549 (Fig. S27A). In contrast, we found that CM-ICG@IrQ + L exhibited very low toxicity to LO2 cells even at high concentrations (Fig. 2E), with cell viability higher than 60% at 50 μg mL^{-1}.

For a deeper understanding of the effect of NQO1 on cell survival upon treating with the nano-prodrugs, the cytotoxicity analysis was performed in A549 cells with NQO1 inhibitor. As shown in Fig. S27B, for both IrQ NPs and CM-ICG@IrQ + L, the survival rate of the cells was much higher than that of A549 cell without the pretreatment of NQO1 inhibitor. Subsequently, Annexin VFITC/Propidium Iodide (PI) apoptosis test was carried out to further explore the capability of our nano-prodrugs in inducing apoptosis. As shown in Fig. 2F, relatively low apoptosis was observed in ICG + L, IrQ NPs and ICG@IrQ, with apoptosis rates (Q2+Q3) at 10.71%, 25.66% and 31.00%, respectively. Due to the integration of ICG and IrQ, the nano-prodrug ICG@IrQ showed relatively high apoptosis with an apoptosis rate at 58.08% upon irradiation. The hybrid membrane coated CM-ICG@IrQ showed the highest apoptosis under irradiation with an apoptosis rate at 69.10%. In addition, the cytotoxic tendency similar to the apoptosis assay results was also demonstrated in the Live/dead cell staining assays. CM-ICG@IrQ + L showed the lowest number of living cells (green fluorescence, Calcein stained living cells) and the highest number of dead cells (red fluorescence, PI stained dead cells), indicating that IrQ combined with ICG and hybrid membrane-promoted targeting resulted in the highest cytotoxicity to A549 cells (Fig. 2G). Rapid internalization of nano-drug is particularly important for efficient induction of cancer cell death. To further demonstrate that the coating of the hybrid membrane can achieve efficient targeting of the corresponding cancer cells, short-term drug administration based on CCK8 was conducted. As shown in Fig. 2H, cells (A549, HeLa, and LO2) were incubated with ICG@IrQ and CM-ICG@IrQ for 4 h, then replace the medicated medium with fresh medium and incubated for another 72 h before the CCK8 assay. We found that CM-ICG@IrQ at the same concentration showed higher cytotoxicity in A549 cells than that in HeLa and LO2 due to homologous targeting of

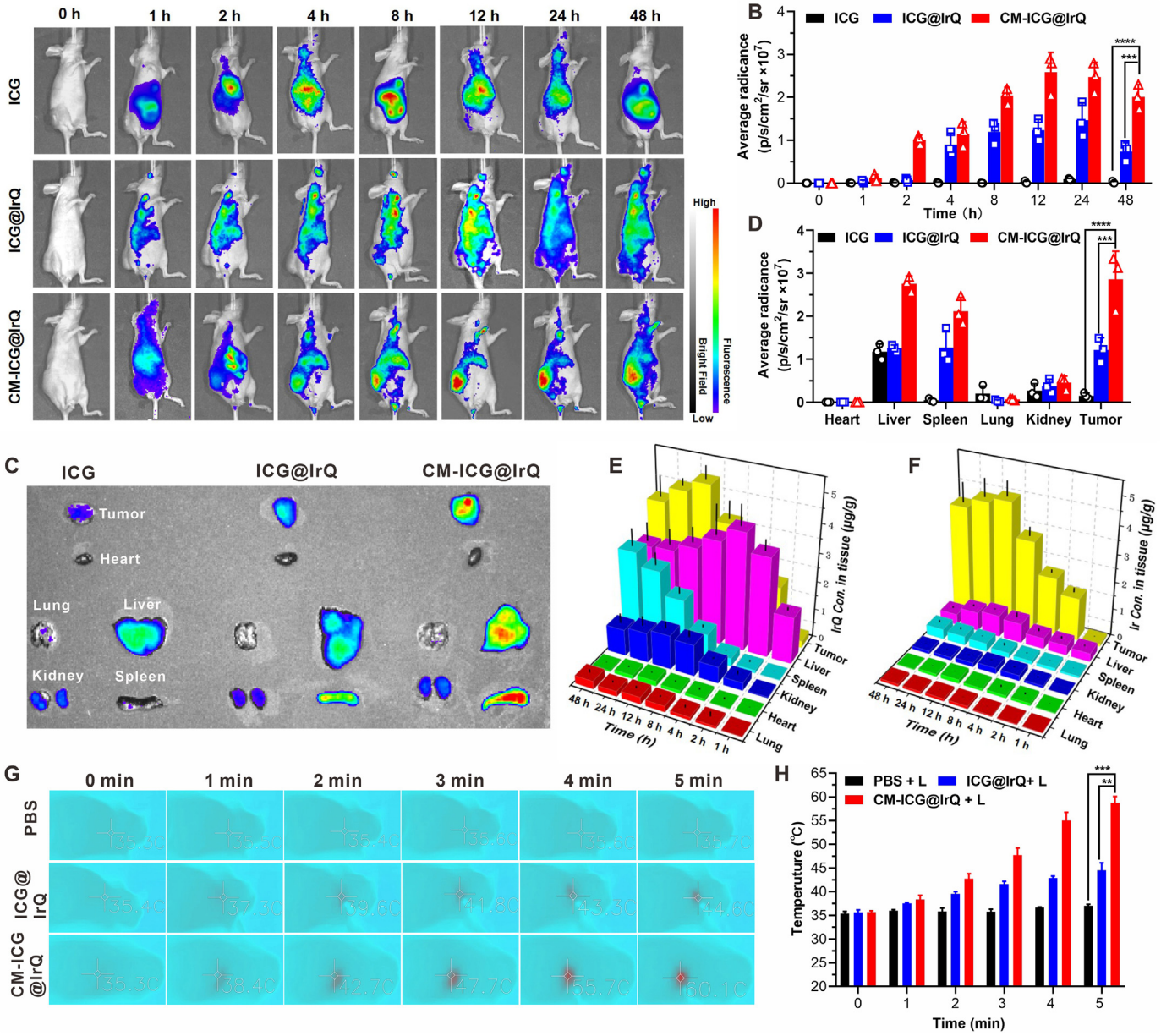

Fig. 3. (A) *In vivo* fluorescence imaging for visualizing the biodistribution of ICG, ICG@IrQ, and CM-ICG@IrQ (ICG dose: 1 mg kg^{-1}). (B) Quantitative analysis of tumor average fluorescence intensities corresponding to (A), n = 3. (C) *Ex vivo* fluorescence imaging of the tumors and various organs after the *in vivo* imaging, n = 3. (D) Quantification of fluorescence intensities of the *ex vivo* fluorescence imaging. (E–F) Quantification of IrQ and Ir in tumors and major organs. (G) Infrared thermal images of the tumor after 12 h administration of PBS, ICG@IrQ and CM-ICG@IrQ (ICG dose: 2 mg kg^{-1}). (H) Temperature statistics of the photothermal imaging. Data are shown as mean ± S.D. **P < 0.01, ***P < 0.001 and ****P < 0.0001 were tested via a two-tailed Student's t-test.

hybrid membranes. Notably, the CM-ICG@IrQ was much more toxic than the ICG@IrQ in A549 cells. However, CM-ICG@IrQ and ICG@IrQ showed slight toxicity to HeLa and LO2 cells, and there was little difference in toxicity at the same concentration. These data demonstrated the advantages of hybrid membrane coated nano-prodrug for ICG@IrQ delivery.

3.6. *In vivo drug release behavior and drug accumulations of CM-ICG@IrQ by fluorescence and photothermal imaging*

Given the efficient homologous targeting of the nano-prodrugs and their excellent antiproliferation activity against NQO1 overexpressed cancer cells, we probed the feasibility of their application *in vivo*. We first evaluated the hemocompatibility of our biomimetic nano-prodrug by hemolysis assay. As shown in Fig. S28, the erythrocytes were incubated with different formulations, and the hemolysis rate represented the hemocompatibility under physiological conditions. Only the hemolysis rate of ICG and ICG@IrQ was higher than 5% with a high concentration (2 mg mL^{-1}), while the membrane coated CM-ICG@IrQ displayed the lowest hemolysis rate, suggesting that the introduction of cell membrane on ICG@IrQ could improve the hemocompatibility. Based on the favourable hemocompatibility of our nano-prodrugs, we further propeled their application *in vivo*. ICG, ICG@IrQ and CM-ICG@IrQ were administrated into A549 tumor-bearing nude mice intravenously. Fluorescence imaging was implemented to record the fluorescence signal of the mice at different time intervals. A discernible fluorescence signal was recorded at the tumor site at 1 h after the administration of CM-ICG@IrQ, increasing steadily and reaching the highest level at 12 h (Fig. 3A and B), and moreover, a strong fluorescence signal was still observed at 48 h. At each observation time point, the fluorescence at the tumor sites was significantly weaker in mice after injection with ICG@IrQ due to the lack of tumor targeting ability. However, negligible fluorescence was detected at tumor sites in free ICG groups due to the rapid blood clearance. After *in vivo* imaging, the mice were sacrificed immediately, and tumor tissues and major organs were dissected for *ex vivo* imaging (Fig. 3C). The fluorescence intensity as shown in Fig. 3C was quantified in Fig. 3D. Tumors of mice in the CM-ICG@IrQ group showed more significant fluorescence than those in the free ICG and ICG@IrQ groups. It was also found that the fluorescence signal of metabolic liver and spleen was stronger than that of other organs. The above data firmly verified that CM-ICG@IrQ can accumulate in tumor tissues selectively.

To investigate the biodistribution of the nano-prodrug and the release efficiency of Ir on tumor-bearing mice, the Ir and IrQ extracted from the tumor and major organs after intravenous administration of CM-ICG@IrQ were quantified. As shown in Fig. 3E, IrQ was mainly accumulated in liver due to the liver first pass effect of its nano-formulation at the early stage of drug administration, and then they gradually reached in tumor tissue *via* active-targeting and EPR effect. In details, the accumulation of IrQ in liver reached the maximum value (4.12 μg g^{-1}) at 4 h after administration, while decreasing gradually to 2.89 μg g^{-1} at 48 h. Simultaneously, IrQ was gradually increased in tumor site and reached highest level (4.92 μg g^{-1}) at 12 h. We found that the biodistribution of IrQ in tumors and organs agree well with the results of *in vivo* and *ex vivo* fluorescence imaging (Fig. 3A–D), which provides an accurate method for monitoring the pharmacokinetic process of this nano-prodrug system. In comparison with IrQ, the accumulation of Ir exhibited the similar result in tumors, which released from IrQ in the presence of overexpressed NQO1. The accumulation of Ir in tumor increased with time, and reached the highest level (4.45 μg g^{-1}) at 12 h after administration (Fig. 3F). Interestingly, the distribution of Ir in various organs showed significantly different from that of IrQ. The content of Ir was very low in the organs, mainly due to the low accumulation level of IrQ in various organs and the lack of NQO1, implying the feasibility of our nano-prodrug system in reducing the side-effects of treatment.

Encouraged by the excellent performance of our biomimetic nano-prodrug in tumor accumulation and efficient activation, we performed photothermal imaging to estimate the photothermal properties of CM-ICG@IrQ in tumor tissues under a laser irradiation (808 nm, 1 W cm^{-2}). 12 h after intravenous administration of PBS, ICG@IrQ and CM-ICG@IrQ to A549 tumor-bearing mice, the tumor sites were irradiated, and the tumor temperature were monitored. As shown in Fig. 3G and H, ICG@IrQ only raised the tumor local temperature to 44.8 °C, whereas CM-ICG@IrQ output more over 60.0 °C within 5 min irradiation that was exceeded the threshold for ablation of cancer cells. Subsequently, we demonstrated the ability of the nano-prodrugs to produce ROS at the tissue level. As is shown in Fig. S29, CM-ICG@IrQ group showed the strongest green fluorescence, which was produced by DCFH-DA in the presence of ROS, indicating that CM-ICG@IrQ could produce significant ROS *in vivo*. These results reliably demonstrated that CM-ICG@IrQ exhibited an outstanding photothermal and photodynamic performance for *in vivo* anticancer treatment.

3.7. *In vivo antitumor efficiency of CM-ICG@IrQ on A549 subcutaneous xenograft model*

To elucidate the potential antitumor effect of CM-ICG@IrQ for NSCLC, the treatment schedule and timeline were rational programmed and illustrated in Fig. 4A. As previously reported, the scarcity of appropriate *in vivo* metabolism characters for free drugs (ICG) treatment caused poor tumor growth inhibition effects as expected [50]. As shown in Fig. 4B–D, with the nano-formulation, ICG@IrQ showed improved chemotherapy effects than PBS or free drug groups because of the combination of chemotherapy and phototherapy. In addition, with the contribution of tumor cell membrane for remarkable tumor cell targeting as we demonstrated *in vitro*, combination therapy in CM-ICG@IrQ + L group resulted in the best tumor burden reduction (Fig. 4B), as 4/5 mice in this group showed tumor volume shrinkage after 24 days observation while 0/5 tumor shrink in any other group (Fig. 4C and D), and as illustrated in Fig. 4E, CM-ICG@IrQ + L group showed the least tumor weight.

As one of the major hurdles for chemotherapy, the severe side-effect of chemotherapeutics causing severe body weight loss restricted its clinical application. Thus, we monitored 24 days of body weight changes with different treatments, and no obvious body weight loss happened except in the ICG + L group (Fig. 4F). In addition, H&E staining images for major organs also showed rare organ damage, confirming the biocompatibility and biosecurity of our nano-prodrugs (Fig. S30). Additionally, the long-term survival rate was counted for 50 days, as shown in Fig. 4G, all mice in CM-ICG@IrQ treatment group survived after 50 days, which implied the excellent combination therapy effect. After 24 days trearments, tumor slices were gained for H&E stained, and we found that the cells of the tumor region harvested from CM-ICG@IrQ + L group showed severe necrosis and shrinkage (Fig. 4H), which further verified the superior therapeutic effect of CM-ICG@IrQ combination therapy of chemo-photo agent.

3.8. *Effect of CM-ICG@IrQ on tumor metastasis inhibition in vivo*

Previous reports demonstrated that nanoparticles could effectively infiltrate into the primary tumor *via* the EPR effects. However, the metastasis tumor node in lung were small clusters with poor vasculature and angiogenic dormancy [52,53]. Thus, it is a challenging to achieve the inhibition of tumor metastases in NSCLC by nano-drug. To further determine whether CM-ICG@IrQ could inhibit the development of lung metastasis tumors, the NSCLC lung metastasis model based on luciferase-expressing A549 cells (A549-Luci) was established to monitor lung metastasis in mice by bioluminescence imaging. The establishment of the lung metastasis model and the treatment process of drug administration were depicted in Fig. 5A. After intravenous injection of A549-Luci cells, mice were treated with PBS, free ICG, IrQ NPs, ICG@IrQ, ICG@IrQ + L, and CM-ICG@IrQ + L, and bioluminescence images were taken on day 4, 12 and 21, respectively. As illustrated in Fig. 5B, we

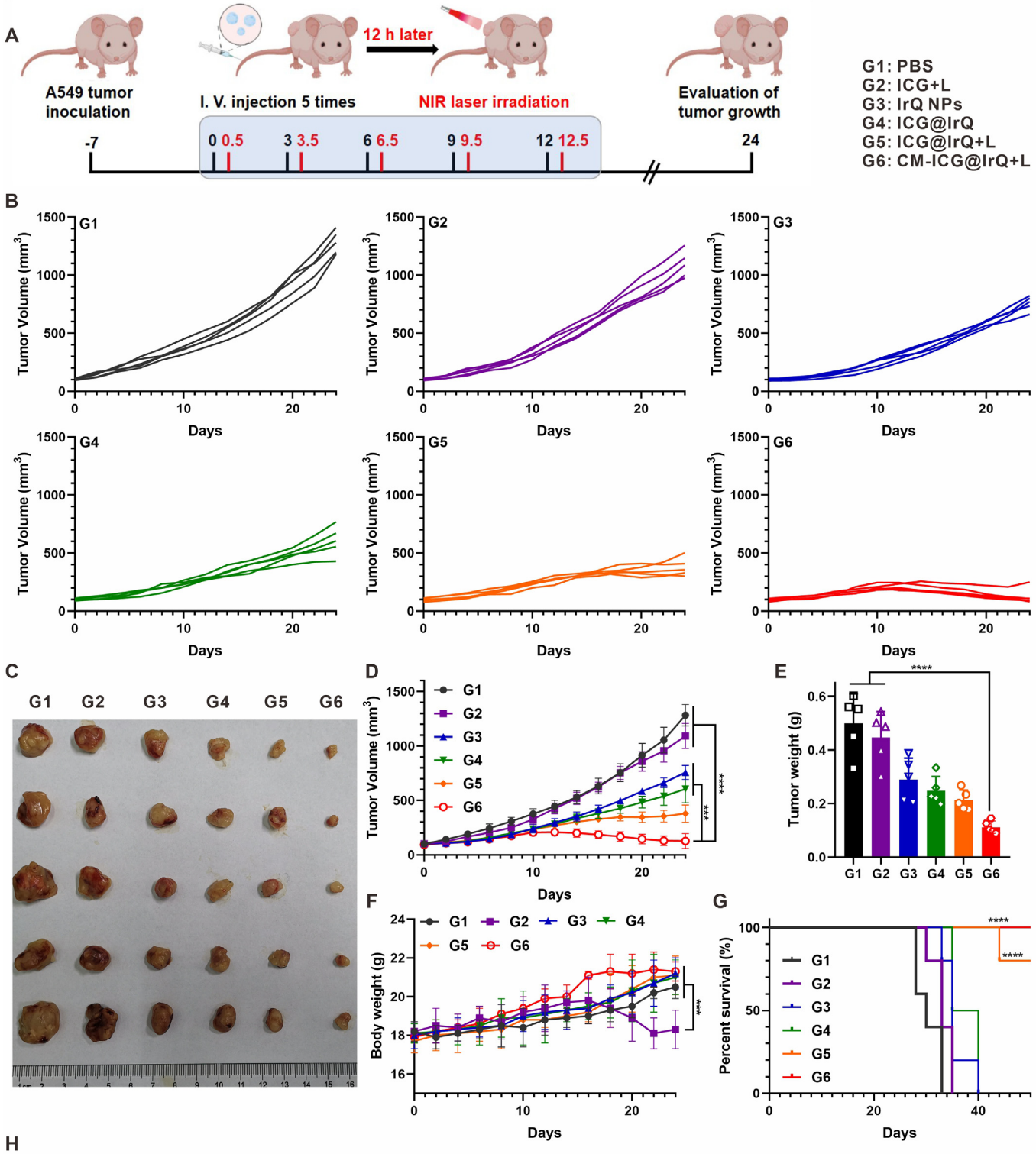

(caption on next page)

Fig. 4. (A) Schedule of treatment for injections and laser irradiations on A549 subcutaneous xenograft model. Different formulations (G1-G6) were administrated on day 0, 3, 6 9 and 12, respectively. The irradiation was performed after 12 h of the administration. (B) Individual tumor volume curves in different groups for 24 days. (G1: PBS, G2: ICG + L, G3: IrQ NPs, G4: ICG@IrQ, G5: ICG@IrQ + L, G6: CM-ICG@IrQ + L). (C) Photographs of the tumors dissected from mice in G1-G6 after 24 days treatment. (D) Statistical tumor volume growth graph of different groups during 24 days treatment. (E) Tumor weight of each group at the end of 24 days treatment. (F) Body weight of mice in each group during 24 days treatment. (G) Survival curve of G1-G6 groups within 50 days. (H) Graphs of typical H&E stained tumor slices from G1 to G6. (scale bar: 200 μm). The sample size is 5 for each group. Data are shown as mean ± S.D. ***P < 0.001 and ****P < 0.0001 were tested via a two-tailed Student's t-test.

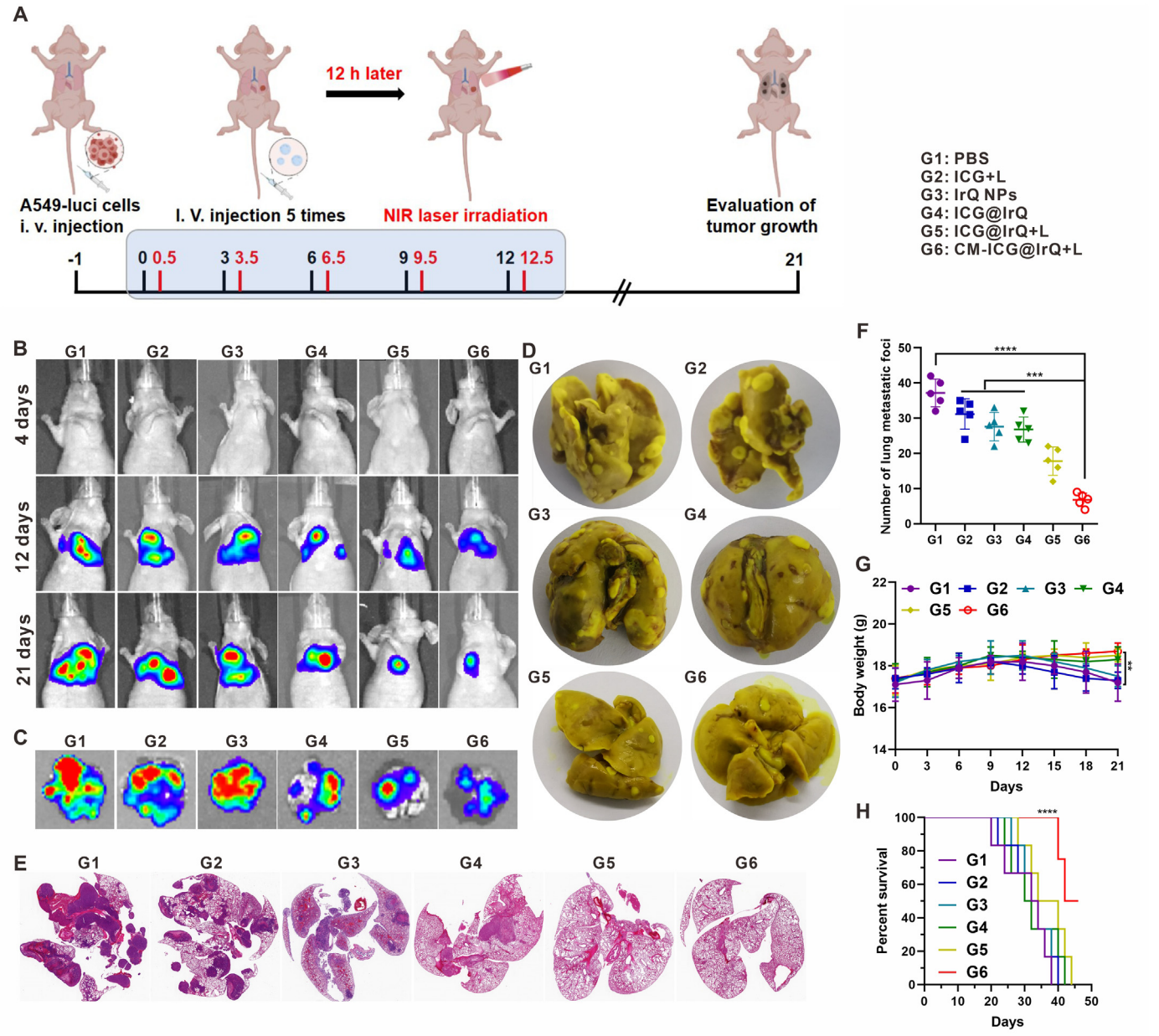

Fig. 5. (A) Schedule of treatment on lung metastasis model. A549-luci cells were intravenous injected on day −1 and different formulations (G1-G6) were administrated on day 0, 3, 6 9 and 12, respectively. The irradiation was performed after 12 h of the administration. (B) Representative *in vivo* bioluminescent images on days 4, 12 and 21. (C) *Ex vivo* bioluminescence imaging for metastasis in the lung on day 21. (D) Representative images of metastasis nodules on lungs by Bouin's fluid staining of G1-G6 on day 21. (E) Representative H&E staining images of lung sections of G1-G6 after 21 days treatment. (F) The number of lung metastatic foci in G1-G6 after 21 days treatment. (G) Body weight of mice in G1-G6 during treatment. (H) Survive curves of mice in lung metastasis model in 45 days. The sample size is 5 for each group. Data are shown as mean ± S.D. ***P < 0.001 and ****P < 0.0001 were tested via a two-tailed Student's t-test.

found that the bioluminescence intensities of lung metastatic foci on CM-ICG@IrQ + L were severely weak than other groups at 21 days treatment, and the bioluminescence of *ex vivo* lungs from different groups also showed the same trend as *in vivo* results (Fig. 5C). Moreover, the obvious nodules could be detected from the lung appearance of each treatment group by Bouin's fluid staining on day 21 (Fig. 5D), but the number of nodules in the CM-ICG@IrQ group (Fig. 5D and F) was less than 10 per mice, and it was significantly lower than that of other groups. As shown in Fig. 5E, the representative H&E staining images further confirmed the therapeutic effects of CM-ICG@IrQ, which displayed

lowest metastasis nodules in all groups. In addition, the body weight of each mouse was monitored during the treatments, and negligible changes were found for the group of CM-ICG@IrQ + L after the course of treatment (Fig. 5G). Furthermore, half mice of the CM-ICG@IrQ + L group survived after 45 days, which indicated the long-term inhibition effect of the nano-prodrugs on metastasis of NSCLC tumor (Fig. 5H). All these results suggested that our biomimetic nano-prodrug could significantly inhibit the tumor metastasis and prolong the survival rate of mice.

4. Conclusion

In summary, we found that a simple insertion of NQO1-responsive quinone propionate into hydrophilic chemotherapeutics Ir could generate an excellent self-assembly behavior by rational drug amphiphile, resulting in the transformation of the small molecular prodrug into a stable and uniform nano-prodrug. Novelty, this self-assembly behavior could load ICG via the reprecipitation method to form a multifunctional nano-prodrug, achieving an efficient combination therapy of chemotherapeutics with PDT/PTT. In addition, this multifunctional nano-prodrug was coated by a hybrid membrane that enhanced the stability in circulation and tumor target capability. In TME, the overexpressed NQO1 triggered the disassembly of this biomimetic nano-prodrug and activated the drug release of Ir and ICG, and the *in vivo* fluorescence imaging revealed that this biomimetic nano-prodrug displayed good active-targeting capacity for tumor accumulation. In the NSCLC mice model, this combination therapy enhanced chemotherapeutic efficacy of Ir on tumor growth inhibition and exhibit a remarkable *in vivo* therapeutics effect with good biosafety, as well as even can suppress tumor metastasis. This combined strategy may provide an alternative and effective approach for NSCLC tumor treatment by simple amphiphile nano-prodrug.

Credit author statement

Peilian Liu: Conceptualization, Formal analysis, Funding acquisition, Investigation, Methodology, Project administration, Writing - original draft; Yong Huang: Funding acquisition, Investigation, Methodology, Resources, Writing - review & editing; Chenyue Zhan: Investigation, Project administration, Resources, Validation, Funding acquisition; Fu Zhang, Chuansen Deng: Investigation, Methodology; Yongmei Jia, Tao Wan: Investigation, Methodology, Resources; Sheng Wang, Bowen Li: Conceptualization, Funding acquisition, Resources, Supervision, Validation, Writing - review & editing.

Declaration of competing interest

The authors declare that they have no known competing financial interests or personal relationships that could have appeared to influence the work reported in this paper.

Data availability

Data will be made available on request.

Acknowledgements

The work was supported by Natural Science Foundation of Guangdong Province (2021A1515010203, 2022A1515011311), Open Project of Key Laboratory of Chean Energy Material Chemistry in Guangdong General University (CEMC2022012), Natural Science Foundation of Lingnan Normal University (ZL1802), China Postdoctoral Science Foundation (2021M702832), Characteristic Innovation Project of Guangdong (2022KTSCX072), Zhejiang Provincial Postdoctoral Research Project Merit-based Funding (ZJ2021054), and National Natural Science Foundation of China (32000992, 21878136, 32101063, 32101124).

Appendix A. Supplementary data

Supplementary data to this article can be found online at https://doi.org/10.1016/j.mtbio.2023.100722.

References

[1] K. Shang, L.P. Zhang, Y.J. Yu, H.H. Xiao, Y.J. Gao, L. Yang, J. Huang, H.Q. Song, H.B. Han, Disulfide-containing polymer delivery of C527 and a Platinum(IV) prodrug selectively inhibited protein ubiquitination and tumor growth on cisplatin resistant and patient-derived liver cancer models, Mater. Today Bio 18 (2023), 100548, https://doi.org/10.1016/j.mtbio.2023.100548.
[2] C. Qian, J.J. Wang, Y. Qian, R.F. Hu, J.Y. Zou, C.Q. Zhu, Y. Zhu, S.Y. Qi, X.B. Jia, L. Wu, W.D. Li, Z.P. Chen, Tumor-cell-surface adherable peptide-drug conjugate prodrug nanoparticles inhibit tumor metastasis and augment treatment efficacy, Nano Lett. 20 (2020) 4153–4161, https://doi.org/10.1021/acs.nanolett.0c00152.
[3] S. Zhou, Q. Shang, N. Wang, Q. Li, A. Song, Y. Luan, Rational design of a minimalist nanoplatform to maximize immunotherapeutic efficacy: four birds with one stone, J. Contr. Release 328 (2020) 617–630, https://doi.org/10.1016/j.jconrel.2020.09.035.
[4] H. Hu, D.F. Xu, Q.B. Xu, Y.X. Tang, J. Hong, Y. Hu, J.H. Wang, X.Y. Ni, Reduction-responsive worm-like nanoparticles for synergistic cancer chemo-photodynamic therapy, Mater, Today Bio 18 (2023), 100542, https://doi.org/10.1016/j.mtbio.2023.100542.
[5] Z.P. Guo, Y.Y. Hu, M.Y. Zhao, K. Hao, P. He, H.Y. Tian, X.S. Chen, M.W. Chen, Prodrug-based versatile nanomedicine with simultaneous physical and physiological tumor penetration for enhanced cancer chemo-immunotherapy, Nano Lett. 21 (2021) 3721–3730, https://doi.org/10.1021/acs.nanolett.0c04772.
[6] P.L. Liu, J.S. Xu, D.H. Yan, P.S. Zhang, F. Zeng, B.W. Li, S.Z. Wu, A DT-diaphorase responsive theranostic prodrug for diagnosis, drug release monitoring and therapy, Chem. Commun. 51 (2015) 9567–9570, https://doi.org/10.1039/c5cc02149a.
[7] E.-J. Kim, S. Bhuniya, H. Lee, H.M. Kim, C. Cheong, S. Maiti, K.S. Hong, J.S. Kim, An activatable prodrug for the treatment of metastatic tumors, J. Am. Chem. Soc. 136 (2014) 13888–13894, https://doi.org/10.1021/ja5077684.
[8] S.Y. Li, L.H. Liu, H.Z. Jia, W.X. Qiu, L. Rong, H. Cheng, X.Z. Zhang, A pH-responsive prodrug for real-time drug release monitoring and targeted cancer therapy, Chem. Commun. 50 (2014) 11852–11855, https://doi.org/10.1039/c4cc05008h.
[9] C.C. Tjin, K.D. Otley, T.D. Baguley, P. Kurup, J. Xu, A.C. Nairn, P.J. Lombroso, J.A. Ellman, Glutathione-responsive selenosulfide prodrugs as a platform strategy for potent and selective mechanism-based inhibition of protein tyrosine phosphatases, ACS Cent. Sci. 3 (2017) 1322–1328, https://doi.org/10.1021/acscentsci.7b00486.
[10] J. Shi, P.W. Kantoff, R. Wooster, O.C. Farokhzad, Cancer nanomedicine: progress, challenges and opportunities, Nat. Rev. Cancer 17 (2017) 20–37, https://doi.org/10.1038/nrc.2016.108.
[11] T.C. Johnstone, K. Suntharalingam, S.J. Lippard, The next generation of platinum drugs: targeted Pt(II) agents, nanoparticle delivery, and Pt(IV) prodrugs, Chem. Rev. 116 (2016) 3436–3486, https://doi.org/10.1021/acs.chemrev.5b00597.
[12] M.T.J. Olesen, R. Walther, P.P. Poier, F. Dagnæs-Hansen, A.N. Zelikin, Molecular, macromolecular, and supramolecular glucuronide prodrugs: lead identified for anticancer prodrug monotherapy, Angew. Chem. Int. Ed. 59 (2020) 7390–7396, https://doi.org/10.1002/anie.201916124.
[13] S.L. Mo, Y. Wen, F.F. Xue, H.C. Lan, Y.Y. Mao, G.L. Lv, T. Yi, A novel O-nitrobenzyl-Based photocleavable antitumor prodrug with the capability of releasing 5-fluorourail, Sci. Bull. 61 (2016) 459–467, https://doi.org/10.1007/s11434-016-1010-5.
[14] D. Cui, , J.G., X. Zhen Huang, J.C. Li, Y.Y. Jiang, K.Y. Pu, A Semiconducting polymer nano-prodrug for hypoxia-activated photodynamic cancer therapy, Angew. Chem. Int. Ed. 58 (2019) 5920–5924, https://doi.org/10.1002/anie.201814730.
[15] A.G. Cheetham, R.W. Chakroun, W. Ma, H.G. Cui, Self-assembling prodrugs, Chem. Soc. Rev. 46 (2017) 6638–6663, https://doi.org/10.1039/c7cs00521k.
[16] H.Z. He, L.H. Du, H.M. Xue, J. Wu, X.T. Shuai, Programmable therapeutic nanoscale covalent organic framework for photodynamic therapy and hypoxia-activated cascade chemotherapy, Acta Biomater. 149 (2022) 297–306, https://doi.org/10.1016/j.actbio.2022.07.003.
[17] P. Tan, X. Chen, H. Zhang, Q. Wei, K. Luo, Artificial intelligence aids in development of nanomedicines for cancer management, Semin. Cancer Biol. 89 (2023) 61–75, https://doi.org/10.1016/j.semcancer.2023.01.005.
[18] H. Li, J. Sun, H. Zhu, H. Wu, H. Zhang, Z. Gu, K. Luo, Recent advances in development of dendritic polymer-based nanomedicines for cancer diagnosis, WIRES Nanomed, Nanobi 13 (2021), e1670, https://doi.org/10.1002/wnan.1670.
[19] Y. Li, Z. Duan, D. Pan, L. Ren, L. Gu, X. Li, G. Xu, H. Zhu, H. Zhang, Z. Gu, R. Chen, Q. Gong, Y. Wu, K. Luo, Attenuating metabolic competition of tumor cells for favoring the nutritional demand of immune cells by a branched polymeric drug delivery system, Adv. Mater. 35 (2023), 2210161, https://doi.org/10.1002/adma.202210161.
[20] K.K. Yang, G.C. Yu, R. Tian, Z.J. Zhou, H.Z. Deng, L. Li, Z. Yang, G.F. Zhang, D.H. Liu, J.W. Wei, L.D. Yue, R.B. Wang, X.Y. Chen, Oxygen-evolving manganese ferrite nanovesicles for hypoxia-responsive drug delivery and enhanced cancer chemoimmunotherapy, Adv. Funct. Mater. 31 (2021), 2008078, https://doi.org/10.1002/adfm.202008078.
[21] M. Lu, X. Huang, X.H. Cai, J.J. Sun, X.M. Liu, L.Y. Weng, L. Zhu, Q.Q. Luo, Z.P. Chen, Hypoxia-responsive stereocomplex polymeric micelles with improved drug loading inhibit breast cancer metastasis in an orthotopic murine model, ACS

Appl. Mater. Interfaces 14 (2022) 20551–20565, https://doi.org/10.1021/acsami.1c23737.
[22] T. Hu, Z. Gu, G.R. Williams, M. Strimaite, J. Zha, Z. Zhou, X. Zhang, C. Tan, R. Liang, Layered double hydroxide-based nanomaterials for biomedical applications, Chem. Soc. Rev. 51 (2022) 6126–6176, https://doi.org/10.1039/d2cs00236a.
[23] Z. Zhou, Y. Wang, F. Peng, F. Meng, J. Zha, L. Ma, Y. Du, N. Peng, L. Ma, Q. Zhang, L. Gu, W. Yin, Z. Gu, C. Tan, Intercalation-activated layered MoO3 nanobelts as biodegradable nanozymes for tumor-specific photo-enhanced catalytic therapy, Angew. Chem. Int. Ed. 61 (2022), e202115939, https://doi.org/10.1002/anie.202115939.
[24] H. Cheng, X.-Y. Jiang, R.-R. Zheng, S.-J. Zuo, L.-P. Zhao, G.-L. Fan, B.-R. Xie, X.-Y. Yu, S.-Y. Li, X.-Z. Zhang, A biomimetic cascade nanoreactor for tumor targeted starvation therapy-amplified chemotherapy, Biomaterials 195 (2019) 75–85, https://doi.org/10.1016/j.biomaterials.2019.01.003.
[25] Y. Bin, J. Gao, Q. Pei, H.X. Xu, H.J. Yu, Engineering prodrug nanomedicine for cancer immunotherapy, Adv. Sci. 7 (2020), 2002365, https://doi.org/10.1002/advs.202002365.
[26] Z. Zhou, B. Li, C. Wu, D. Shen, H. Fan, J. Zhao, H. Li, Z. Zeng, Z. Luo, L. Ma, C. Tan, Metallic 1T phase enabling MoS2 nanodots as an efficient agent for photoacoustic imaging guided photothermal therapy in the near-infrared-II window, Small 16 (2020), 2004173, https://doi.org/10.1002/smll.202004173.
[27] T. Hu, Q. Liu, Z. Zhou, H. Huang, F. Meng, W. Liu, Q. Zhang, L. Gu, R. Liang, C. Tan, Preparation of dye molecule-intercalated MoO3 organic/inorganic superlattice nanoparticles for fluorescence imaging-guided catalytic therapy, Small 18 (2022), 2200595, https://doi.org/10.1002/smll.202200595.
[28] Q. Wang, M. Xiao, D.Y. Wang, X.X. Hou, J. Gao, J.J. Liu, J.F. Liu, In situ supramolecular self-assembly of Pt(IV) prodrug to conquer cisplatin resistance, Adv. Funct. Mater. 31 (2021), 2101826, https://doi.org/10.1002/adfm.202101826.
[29] Y.X. Yang, B.J. Sun, S.Y. Zuo, X.M. Li, S. Zhou, L.X. Li, C. Luo, H.Z. Liu, M.S. Cheng, Y.J. Wang, S.J. Wang, Z.G. He, J. Sun, Trisulfide bond-mediated doxorubicin dimeric prodrug nanoassemblies with high drug doading, high self-assembly sstability, and high tumor selectivity, Sci. Adv. 6 (2020), https://doi.org/10.1126/sciadv.abc1725 eabc1725.
[30] J.Q. Lu, C. Liu, P.C. Wang, M. Ghazwani, J.N. Xu, Y.X. Huang, X.C. Ma, P.J. Zhang, S. Li, The self-assembling camptothecin-tocopherol prodrug: an effective approach for formulating camptothecin, Biomaterials 62 (2015) 176–187, https://doi.org/10.1016/j.biomaterials.2015.05.046.
[31] B.J. Sun, C. Luo, X.B. Zhang, M.R. Guo, M.C. Sun, H. Yu, Q. Chen, W.Q. Yang, M.L. Wang, S.Y. Zuo, P.Y. Chen, Q.M. Kan, H.T. Zhang, Y.J. Wang, Z.G. He, J. Sun, Probing the impact of sulfur/selenium/carbon linkages on prodrug nanoassemblies for cancer therapy, Nat. Commun. 10 (2019) 3211, https://doi.org/10.1038/s41467-019-11193-x.
[32] G.Q. Ma, J. Liu, J.L. He, M.Z. Zhang, P.H. Ni, Dual-responsive polyphosphoester-doxorubicin prodrug containing a diselenide bond: synthesis, characterization, and drug delivery, ACS Biomater. Sci. Eng. 4 (2018) 2443–2452, https://doi.org/10.1021/acsbiomaterials.8b00429.
[33] C.Y. Zhan, G.F. Lin, Y. Huang, Z.Q. Wang, F. Zeng, S.Z. Wu, Dopamine-precursor-based nanoprodrug for in-situ drug release and treatment of acute liver failure by inhibiting NLRP3 inflammasome and facilitating liver regeneration, Biomaterials 268 (2021), 120573, https://doi.org/10.1016/j.biomaterials.2020.120573.
[34] H. Liang, Z.W. Zhou, R.J. Luo, M.M. Sang, B.W. Liu, M.J. Sun, W. Qu, F. Feng, W.Y. Liu, Tumor-specific activated photodynamic therapy with an oxidation-regulated strategy for enhancing anti-tumor efficacy, Theranostics 8 (2018) 5059–5071, https://doi.org/10.7150/thno.28344.
[35] D.-B. Cheng, D. Wang, Y.-J. Gao, L. Wang, Z.-Y. Qiao, H. Wang, Autocatalytic morphology transformation platform for targeted drug accumulation, J. Am. Chem. Soc. 141 (2019) 4406–4411, https://doi.org/10.1021/jacs.8b13512.
[36] P. Huang, D.L. Wang, Y. Su, W. Huang, Y.F. Zhou, D.X. Cui, X.Y. Zhu, D.Y. Yan, Combination of small molecule prodrug and nanodrug delivery: amphiphilic drug-drug conjugate for cancer therapy, J. Am. Chem. Soc. 136 (2014) 11748–11756, https://doi.org/10.1021/ja505212y.
[37] Y. Guo, K. Jiang, Z.C. Shen, G.R. Zheng, L.L. Fan, R.R. Zhao, J.W. Shao, A small molecule nanodrug by self-assembly of dual anticancer drugs and photosensitizer for synergistic near-infrared cancer theranostics, ACS Appl. Mater. Interfaces 9 (2017) 43508–43519, https://doi.org/10.1021/acsami.7b14755.
[38] I.-C. Sun, H.Y. Yoon, D.-K. Lim, K. Kim, Recent trends in in situ enzyme-activatable prodrugs for targeted cancer therapy, Bioconjugate Chem. 31 (2020) 1012–1024, https://doi.org/10.1021/acs.bioconjchem.0c00082.
[39] A. Sharma, E.J. Kim, H. Shi, J.Y. Lee, B.G. Chung, J.S. Kim, Development of a theranostic prodrug for colon cancer therapy by combining ligand-targeted delivery and enzyme-stimulated activation, Biomaterials 155 (2018) 145–151, https://doi.org/10.1016/j.biomaterials.2017.11.019.
[40] G. Tedeschi, S. Chen, V. Massey, DT-diaphorase. Redox potential, steady-state, and rapid reaction studies, J. Biol. Chem. 270 (1995) 1198–1204, https://doi.org/10.1074/jbc.270.3.1198.
[41] A.M. Malkinson, D. Siegel, G.L. Forrest, A.F. Gazdar, H.K. Oie, D.C. Chan, P.A. Bunn, M. Mabry, D.J. Dykes, S.D. Harrison, D. Ross, Elevated DT-diaphorase activity and messenger RNA content in human non-small cell lung carcinoma: relationship to the response of lung tumor xenografts to mitomycin C1, Cancer Res. 52 (1992) 4752–4757. https://aacrjournals.org/cancerres/article/52/17/4752/498116.
[42] X.G. Li, Z.D. Liu, A.L. Zhang, C.H. Han, A.J. Shen, L.X. Jiang, D.A. Boothman, J. Qiao, Y. Wang, X.M. Huang, Y.-X. Fu, NQO1 targeting prodrug triggers innate sensing to overcome checkpoint blockade resistance, Nat. Commun. 10 (2019) 3251, https://doi.org/10.1038/s41467-019-11238-1.
[43] Q.J. Gong, X. Li, T. Li, X.S. Wu, J.B. Hu, F.L. Yang, X.J. Zhang, A carbon-carbon bond cleavage-based prodrug activation strategy applied to β-lapachone for cancer-specific targeting, Angew. Chem. Int. Ed. 61 (2022), e202210001, https://doi.org/10.1002/anie.202210001.
[44] K.W. Wang, X. Xiao, Y. Liu, Q.Y. Zong, Y.L. Tu, Y.Y. Yuan, Self-immolative polyprodrug-based tumor-specific cascade amplificated drug release nanosystem for orchestrated synergistic cancer therapy, Biomaterials 289 (2022), 121803, https://doi.org/10.1016/j.biomaterials.2022.121803.
[45] Z. Xie, T. Fan, J. An, W. Choi, Y. Duo, Y. Ge, B. Zhang, G. Nie, N. Xie, T. Zheng, Y. Chen, H. Zhang, J.S. Kim, Emerging combination strategies with phototherapy in cancer nanomedicine, Chem. Soc. Rev. 49 (2020) 8065–8087, https://doi.org/10.1039/D0CS00215A.
[46] L. Zhu, Y. Zhong, S. Wu, M. Yan, Y. Cao, N. Mou, G. Wang, D. Sun, W. Wu, Cell membrane camouflaged biomimetic nanoparticles: focusing on tumor theranostics, Mater. Today Bio 14 (2022), 100228, https://doi.org/10.1016/j.mtbio.2022.100228.
[47] Q. Li, Y. Zhou, W. He, X. Ren, M. Zhang, Y. Jiang, Z. Zhou, Y. Luan, Platelet-armored nanoplatform to harmonize janus-faced IFN-γ against tumor recurrence and metastasis, J. Contr. Release 338 (2021) 33–45, https://doi.org/10.1016/j.jconrel.2021.08.020.
[48] H.L. Tang, Y.N. Xue, B.W. Li, X.J. Xu, F. Zhang, J.J. Guo, Q.J. Li, T.T. Yuan, Y. Chen, , Y.B. P, Y. Ping, D. Li, Membrane-camouflaged supramolecular nanoparticles for co-delivery of chemotherapeutic and molecular-targeted drugs with siRNA against patient-derived pancreatic carcinoma, Acta Pharm. Sin. B 12 (2022) 3410–3426, https://doi.org/10.1016/j.apsb.2022.02.007.
[49] C.Z. Yao, Y.M. Li, Z.X. Wang, C.Z. Song, X.L. Hu, S.Y. Liu, Cytosolic NQO1 enzyme-activated near-infrared fluorescence imaging and photodynamic therapy with polymeric vesicles, ACS Nano 14 (2020) 1919–1935, https://doi.org/10.1021/acsnano.9b08285.
[50] F. Yan, H. Wu, H.M. Liu, Z.T. Deng, H. Liu, W.L. Duan, X. Liu, H.R. Zheng, Molecular imaging-guided photothermal/photodynamic therapy against tumor by iRGD-modified indocyanine green nanoparticles, J. Contr. Release 224 (2016) 217–228, https://doi.org/10.1016/j.jconrel.2015.12.050.
[51] Y.L. Liu, X. Zhi, M. Yang, J.P. Zhang, L.N. Lin, X. Zhao, W.X. Hou, C.L. Zhang, Q. Zhang, F. Pan, G. Alfranca, Y.M. Yang, J.M. de la Fuente, J. Ni, D.X. Cui, Tumor-triggered drug release from calcium carbonate-encapsulated gold nanostars for near-infrared photodynamic/photothermal combination antitumor therapy, Theranostics 7 (2017) 1650–1662, https://doi.org/10.7150/thno.17602.
[52] T.Q. Lang, X.Y. Dong, Z. Zheng, Y.R. Liu, G.R. Wang, Q. Yin, Y.P. Li, Tumor microenvironment-responsive docetaxel-loaded micelle combats metastatic breast cancer, Sci. Bull. 64 (2019) 91–100, https://doi.org/10.1016/j.scib.2018.12.025.
[53] T. Wan, Q. Pan, C.Y. Liu, J.J. Guo, B.W. Li, X.J. Yan, Y.Y. Cheng, Y. Ping, A duplex CRISPR-cas9 ribonucleoprotein nanomedicine for colorectal cancer gene therapy, Nano Lett. 21 (2021) 9761–9771, https://doi.org/10.1021/acs.nanolett.1c03708.